# Boreal summer intraseasonal oscillations in the MJO skeleton model with observation-based forcing

H. Reed Ogrosky · Samuel N. Stechmann · Andrew J. Majda

Received: date / Accepted: date

Abstract The Madden-Julian oscillation (MJO) skeleton model is a low-order model for intraseasonal oscillations that, in an extended form, includes off-equatorial and antisymmetric components. Previous studies of this extended model have used an idealized background state and forcing terms. In the current study, observation-based estimates of these forcing terms and background state are used. Linear solutions to the extended model with this observation-based forcing consist of both equatorially-symmetric convective events and events with a meridional tilt reminiscent of composites of the boreal summer intraseasonal oscillation (BSISO) in observational studies. Solutions to a nonlinear stochastic form of the model exhibit realistic precipitation mean and variance and intraseasonal variability throughout much of the tropics. These solutions contain several types of events, including meridionally-tilted convective activity that moves both northward and eastward. Solutions to both forms of the model also indicate that this BSISO-like convective activity is coupled to activity over the eastern Pacific. A discussion of these features and their agreement with previous observational studies of the BSISO is given.

## **Keywords**

# 1 Introduction

The primary features of tropical intraseasonal oscillations have been shown to be largely dependent on the season. During boreal winter, the Madden-Julian oscillation (MJO) is a planetary-scale equatorial wave that consists of an envelope of convective activity, approximately symmetric about the equator, that propagates eastward from the Indian ocean to the western Pacific ocean (Madden and Julian, 1971; Hendon and Salby, 1994; Wheeler and Hendon, 2004; Zhang, 2005).

During boreal summer, the focus of the current study, intraseasonal oscillations typically exhibit different features than their wintertime counterparts. Observed events have been examined by means of many data analysis techniques, including lag-regression composites (Lawrence and Webster, 2002; Ajayamohan and Goswami, 2007), empirical orthogonal functions (EOFs) (Lee et al., 2013), extended EOFs (EEOFs) or singular spectrum analysis (Kikuchi et al., 2012), and nonlinear Laplacian spectral analysis (Szekely et al., 2015, 2016). While each of these techniques draws attention to slightly different features of the spatial and temporal characteristics of boreal summer intraseasonal oscillations (BSISOs), there are common features that have been clearly identified by all these techniques including (i) the prevalence of meridionally-tilted (northwest-southeast) convective events organizing in the Indian ocean and

Department of Mathematics, University of Wisconsin-Madison, Madison, WI 53706 E-mail: ogrosky@wisc.edu

## S. N. Stechmann

Department of Mathematics and Department of Atmospheric and Oceanic Sciences, University of Wisconsin-Madison, Madison, WI 53706

## A. J. Majda

Department of Mathematics and Center for Atmosphere Ocean Science, Courant Institute of Mathematical Sciences, New York University, New York, NY 10012

H. R. Ogrosky

moving both across the maritime continent and into the Bay of Bengal and India, and (ii) the northward and eastward propagation of convection associated with the BSISO. It is important to note that of course while these features are clearly identifiable in composites, there is a large degree of variability in the propagation characteristics of individual events during both boreal winter and summer (Wang and Rui, 1990).

General circulation models (GCMs) have traditionally struggled to produce realistic magnitude and location of tropical intraseasonal variability in these regions, both in boreal winter (Lin et al., 2006; Sperber and Kim, 2012) and summer (Ajayamohan and Goswami, 2007), though recent studies have shown that including more sophisticated convective parameterization schemes results in more realistic variability; see, e.g., Ajayamohan et al. (2014). These difficulties extend to other regions of the tropics like the eastern Pacific (Jiang et al., 2013), where convective activity and hurricane formation has been shown to be connected to intraseasonal variability in the eastern hemisphere (Maloney and Hartmann, 2000; Maloney and Kiehl, 2002; Jiang et al., 2014). This underrepresentation of intraseasonal variability is one of the motivations for the creation and study of low-dimensional models for intraseasonal oscillations like the MJO and BSISO.

One of these low-dimensional models is the MJO skeleton model first introduced by Majda and Stechmann (2009, 2011). The model is a nonlinear oscillator model which depicts the MJO as a neutrally-stable planetary-scale wave envelope forced by background latent heating and radiative cooling; no dissipation is included in the model, and the synoptic-scale convective activity is not explicitly resolved. A stochastic birth-death process was added to the model by Thual et al. (2014) to allow for interaction between the resolved planetary-scale dynamics and the unresolved synoptic-scale convective activity. In the simplest form of this model, the model is truncated to a system of four coupled PDEs governing the evolution of the leading meridional mode symmetric about the equator. This produces events with the large-scale structure and propagation of observed MJOs (Hendon and Salby, 1994; Wheeler and Hendon, 2004; Zhang, 2005); see also Stachnik et al. (2015) for a discussion of the model's ability to capture MJO initiation and termination.

Extended forms of the model that include both equatorially symmetric and antisymmetric components may be constructed by truncating the model at higher meridional mode number. Solutions to these 'extended' models produce a greater variety of types of intraseasonal oscillations (Thual et al., 2015). Some of these solutions exhibit structure and behavior similar to the BSISO, including northwest-to-southeast meridional tilts, convective activity centered off the equator, and propagation in both the zonal and meridional direction (Lawrence and Webster, 2002).

Most previous studies of the skeleton model, including all studies of the extended form of the model, have used idealized forcing terms. Specifically, equal latent heating and radiative cooling terms have been prescribed as constants or simple sinusoids representing an idealized warm pool (Majda and Stechmann, 2009, 2011; Thual et al., 2014). In contrast, Ogrosky and Stechmann (2015a) calculated observation-based estimates of the forcing terms for the single-mode skeleton model using reanalysis latent heat net flux, precipitation, and outgoing longwave radiation (OLR) data. In addition to features of previously found solutions, the observation-based model solutions also exhibited a realistic wave envelope of activity centered over the Pacific warm pool. This method was motivated in part by the success of Stechmann and Ogrosky (2014) in using OLR to estimate total diabatic heating in a study of the Walker circulation.

In the current study we provide an observation-based estimate of the extended model's forcing terms using methods similar, though not identical, to those of Ogrosky and Stechmann (2015a) and study the behavior of solutions to both the linear deterministic and nonlinear stochastic versions of the model. It will be shown that the resulting solutions exhibit several of the key features of the BSISO discussed above. Specifically, the model produces (i) convective activity that has reasonably realistic intraseasonal variability throughout much of the tropics, especially the Asian monsoon region, (ii) meridionally-tilted (northwest-southeast) events, and (iii) both northward and eastward propagation of intraseasonal rainfall anomalies. These features will be shown to exist in both linear and (nonlinear) stochastic model solutions. In addition, the nonlinear stochastic simulations produce climatological statistics of precipitation mean and variance that have many features in common with observed statistics.

The rest of the paper is organized as follows: in Sect. 2, the skeleton model and some solutions are reviewed. The data and methods used in the current study are discussed in Sect. 3. Solutions to the nonlinear stochastic extended skeleton model are discussed in Sect. 4, and solutions to the linearized deterministic version are discussed in Sect. 5. A brief discussion of the sensitivity of the results to parameter choices is given in Sect. 6, and conclusions and acknowledgments are in Sect. 7.

## 2 Model

We first briefly review the skeleton model in its deterministic nonlinear, deterministic linearized, and stochastic nonlinear forms.

## 2.1 Deterministic skeleton model

The MJO skeleton model is a simple nonlinear oscillator model coupling a Matsuno-Gill-like model for winds and potential temperature with no damping to an evolution equation for lower tropospheric moisture and an evolution equation for the wave envelope of convective activity. The model uses a vertical truncation with only the first baroclinic mode retained, i.e.  $u(x, y, z, t) = \sqrt{2}u^*(x, y, t)\cos(z)$ , etc., so that (dropping stars for ease of notation)

$$u_t - yv - \theta_x = 0, (2.1a)$$

$$yu - \theta_y = 0, (2.1b)$$

$$\theta_t - u_x - v_y = \bar{H}a - s^\theta, \tag{2.1c}$$

$$q_t - \tilde{Q}(u_x + v_y) = -\bar{H}a + s^q, \tag{2.1d}$$

$$a_t = \Gamma q a, \tag{2.1e}$$

where  $(u, v, \theta, q, a)$  represent zonal and meridional winds, potential temperature, lower tropospheric moisture, and the planetary-scale wave envelope of convective activity, respectively. The equations (2.1) have been nondimensionalized by standard reference scales; see, e.g., Stechmann and Majda (2015). Equations (2.1a)-(2.1c) are the equatorial long-wave equations and represent the dry dynamics, while the variables q and a are included to represent moist convective processes. Equations (2.1d)-(2.1e) govern the model interaction between moisture anomalies and convective activity. Equation (2.1e) is the simplest equation that encapsulates the observation that anomalies in lower tropospheric moisture tend to lead anomalies in convective activity (Myers and Waliser, 2003); this equation was originally proposed by Majda and Stechmann (2009). Note that the only nonlinearity in the model is the qa term in (2.1e). There are a minimal number of dimensionless model parameters:  $\bar{H} \approx 0.22$  is a constant heating rate prefactor,  $\tilde{Q} = 0.9$  is a background vertical moisture gradient,  $\Gamma$  is a growth/decay rate of the wave envelope of convective activity,  $s^{\theta}(x,y)$  is the radiative cooling rate, and  $s^{q}(x,y)$  is a moistening term.

The model (2.1) can be simplified further by expressing each of the variables and forcing functions as a linear combination of parabolic cylinder functions, e.g.,

$$u(x, y, t) = \sum_{m=0}^{\infty} u_m(x, t)\phi_m(y),$$
 (2.2)

where  $\phi_m$  is the m-th parabolic cylinder function, the first few of which are

$$\phi_0(y) = \frac{1}{\pi^{1/4}} e^{-y^2/2}, \tag{2.3a}$$

$$\phi_1(y) = \frac{1}{\pi^{1/4}} \frac{1}{\sqrt{2}} 2y e^{-y^2/2},\tag{2.3b}$$

$$\phi_2(y) = \frac{1}{\pi^{1/4}} \frac{1}{2\sqrt{2}} (4y^2 - 2) e^{-y^2/2}.$$
 (2.3c)

These parabolic cylinder functions comprise a natural set of basis functions in the meridional direction. Substituting (2.2) and analogous expressions for the other variables and forcing terms into (2.1) results in an infinite set of systems of equations for the spectral coefficients  $u_m$ ,  $v_m$ , etc., with each system coupled to the others only through the nonlinear qa term. As with the Matsuno-Gill model, solutions to these systems are readily found by defining characteristic variables  $r_m = (u_m - \theta_m)/\sqrt{2}$  and  $l_m = (u_m + \theta_m)/\sqrt{2}$  (Matsuno, 1966; Gill, 1980; Majda, 2003). Here, we will take the additional step of defining wave variables K and  $R_m$  by

$$K = r_0, R_m = \sqrt{m+1}r_{m+1} - \sqrt{m}l_{m-1}, (2.4)$$

where K represents the amplitude of the Kelvin wave, and  $R_m$  represents the amplitude of the m-th Rossby wave. The model equations and results shown here will be given in terms of either wave variables K,  $R_m$ , etc., or the primitive variables  $(u, v, \theta, q, a)$ .

The model (2.1) can now be truncated at any desired meridional mode. The simplest form of the skeleton model can be found by using a meridional truncation retaining only K,  $R_1$ ,  $q_0$ , and  $a_0$ :

$$K_t + K_x = -\frac{1}{\sqrt{2}}(\bar{H}A - S^{\theta}),$$
 (2.5a)

$$R_t - \frac{1}{3}R_x = -\frac{2\sqrt{2}}{3}(\bar{H}A - S^{\theta}),$$
 (2.5b)

$$Q_t + \frac{\tilde{Q}}{\sqrt{2}}K_x - \frac{\tilde{Q}}{6\sqrt{2}}R_x = \frac{\tilde{Q}}{6}(\bar{H}A - S^{\theta}) - \bar{H}A + S^q,$$
 (2.5c)

$$A_t = \Gamma(Q - Q_A)A,\tag{2.5d}$$

where we have used R to denote  $R_1$  for simplicity,  $Q = q_0$ ,  $A = a_0$ ,  $S^{\theta} = s_0^{\theta}$  and  $S^q = s_0^q$ . The radiative cooling term  $S^{\theta}$  appears in the moisture equation due to the  $\tilde{Q}v_y$  term in (2.1d). This model has solutions that are symmetric about the equator, and some of its solutions have been shown to exhibit many features of the boreal winter MJO (Majda and Stechmann, 2009, 2011).

Recently the model was studied with a truncation that retained both symmetric and antisymmetric components (Thual et al., 2015). Using the notation and scaling used in Majda and Stechmann (2009), the expanded model may be written as

$$\partial_{t}K + \partial_{x}K = -\frac{1}{\sqrt{2}} \left( \bar{H}A_{0} - S_{0}^{\theta} \right),$$

$$(2.6a)$$

$$\partial_{t}R_{m} - \frac{1}{2m+1} \partial_{x}R_{m} = -\frac{(m+1)\sqrt{2m}}{2m+1} \left( \bar{H}A_{m-1} - S_{m-1}^{\theta} \right)$$

$$-\frac{2m\sqrt{m+1}}{(2m+1)\sqrt{2}} \left( \bar{H}A_{m+1} - S_{m+1}^{\theta} \right), 1 \leq m \leq M_{R} + 1,$$

$$(2.6b)$$

$$\partial_{t}Q_{0} + \frac{\tilde{Q}}{\sqrt{2}}\partial_{x}K - \frac{\tilde{Q}}{6\sqrt{2}}\partial_{x}R_{1} = -\left(\bar{H}A_{0} - S_{0}^{q}\right) + \frac{\tilde{Q}}{6}\left(\bar{H}A_{0} - S_{0}^{\theta}\right) - \frac{\tilde{Q}}{3\sqrt{2}}\left(\bar{H}A_{2} - S_{2}^{\theta}\right), \quad (2.6c)$$

$$\partial_{t}Q_{m} + \left(-\frac{\tilde{Q}}{2\sqrt{2m+2}} + \frac{\tilde{Q}\sqrt{m+1}}{\sqrt{2}(2m+3)}\right)\partial_{x}R_{m+1} + \left(\frac{\tilde{Q}}{2\sqrt{2m}} - \frac{\tilde{Q}\sqrt{m}}{\sqrt{2}(2m-1)}\right)\partial_{x}R_{m-1}$$

$$= -\left(\bar{H}A_{m} - S_{m}^{q}\right) + \left(\frac{\tilde{Q}m}{4m-2} + \frac{\tilde{Q}(m+1)}{4m+6}\right)\left(\bar{H}A_{m} - S_{m}^{\theta}\right)$$

$$-\frac{\tilde{Q}\sqrt{m}\sqrt{m-1}}{4m-2}\left(\bar{H}A_{m-2} - S_{m-2}^{\theta}\right)$$

$$-\frac{\tilde{Q}\sqrt{m+1}\sqrt{m+2}}{4m+6}\left(\bar{H}A_{m+2} - S_{m+2}^{\theta}\right), \quad 1 \le m \le M_{A},$$

$$(2.6d)$$

$$\partial_t A_m = \Gamma \sum_{i=0}^{M_A} \sum_{j=0}^{M_A} \tilde{\phi}_{ijm} Q_i A_j, \quad 0 \le m \le M_A, \tag{2.6e}$$

where  $M_R+1$  is the number of Rossby modes  $R_1,...,R_{M_R+1}$  retained,  $M_A+1$  is similarly the number of Q's and A's retained, i.e.  $Q_0,...,Q_{M_A}$  and  $A_0,...,A_{M_A}$ , and where  $R_0$  in (2.6d),  $R_i$  for  $i>R_M+1$  and  $A_j$  for  $j>M_A$  in (2.6b) and (2.6d) are all understood to be zero. The study of Thual et al. (2015) showed results for the case  $M_A=4$  and  $M_R=2$ . Here, in order to allow for more refined meridional structures, we present results for  $M_A=M_R=9$ . Finally, the coefficients of the components of the nonlinear term in (2.6e) are given by

$$\tilde{\phi}_{ijm} = \int_{-\infty}^{\infty} \phi_i \phi_j \phi_m \, dy. \tag{2.7}$$

We note that  $\tilde{\phi}_{ijm} \neq 0$  if and only if i + j + m is even, and we also note that the scaling used here is slightly different than that of Thual et al. (2015).

## 2.2 Deterministic model solutions and linearized model

Next, steady-state Walker circulations and linear solutions to the extended skeleton model (2.6) are discussed. As with the single-meridional-mode truncation case considered in Ogrosky and Stechmann (2015a), each of the variables K,  $R_m$ , and  $A_m$  may be expressed as the sum of a background component and anomalies, i.e.

$$K = \bar{K}(x) + K_*(x,t), \quad R_m = \bar{R}_m(x) + R_{m_*}(x,t), \quad A_m = \bar{A}_m(x) + A_{m_*}(x,t),$$
 (2.8)

where an overbar above a function denotes the steady-state, time-independent component of the variable. Lower tropospheric moisture Q is here taken to represent anomalies only, i.e.  $Q = Q_*(x,t)$ , though inclusion of a background state is not inconsistent with the model. In order for a steady-state solution to exist in the absence of dissipative mechanisms, it must be the case that

$$\int_{0}^{P_{E}} \bar{H}\bar{A}_{m} dx = \int_{0}^{P_{E}} S_{m}^{\theta} dx = \int_{0}^{P_{E}} S_{m}^{q} dx, \tag{2.9}$$

for every m (Majda and Klein, 2003). Each mode of the resulting background state of convective activity is given by

$$\bar{H}\bar{A}_{m}(x) = \frac{S_{m}^{q}(x) - \tilde{Q}S_{m}^{\theta}(x)}{1 - \tilde{Q}};$$
(2.10)

the total background state can be recovered by  $\bar{H}\bar{A}(x,y) = \sum_{m=0}^{\bar{M}_A} \bar{H}\bar{A}_m(x)\phi_m(y)$ , and the background Kelvin and m-th Rossby waves may be recovered by integrating the appropriate meridional modes of the background convective state according to (2.6a)-(2.6b). This background flow represents the model's Walker circulation.

To obtain a linearized system, one can remove the background state from the equations, and the anomalies are then governed by (dropping stars hereafter) equations (2.6a)-(2.6d) and

$$\partial_t A_m = \Gamma \sum_{i=0}^{M_A} \sum_{j=0}^{M_A} \tilde{\phi}_{ijm} Q_i (\bar{A}_j + A_j), \quad 0 \le m < M_A,$$
 (2.11)

so that the background state affects the anomalies only through the nonlinearity in the  $A_m$  equations. As long as the anomalies are small compared with the background state at all times and locations, i.e.  $A_m \ll \bar{A}_m$ , then the nonlinear terms  $Q_i A_j$  may be neglected, resulting in a system of linear equations, namely (2.6a)-(2.6d) and

$$\partial_t A_m = \Gamma \sum_{i=0}^{M_A} \sum_{j=0}^{M_{\bar{A}}} \tilde{\phi}_{ijm} Q_i \bar{A}_j, \quad 0 \le m < M_A, \tag{2.12}$$

where  $M_{\bar{A}} \geq 0$  gives the truncation of the background state. The solutions to (2.6a)-(2.6d) and (2.12) will be discussed in Sect. 5.

## 2.3 Stochastic skeleton model

The deterministic formulation of the skeleton model just discussed produces planetary-scale intraseasonal variability and leaves details of the synoptic-scale convective activity unresolved. To account for the effects of smaller-scale convective processes on the intraseasonal variability modeled here, the skeleton model has recently been updated to include a stochastic parameterization of these processes (Thual et al., 2014, 2015). Specifically, a stochastic birth-death process that governs the evolution of the wave envelope A

was added to the model by defining a random variable  $a = \Delta a \eta$  where  $\eta$  is a non-negative integer and  $\Delta a$  is a fixed step size. The probability of a given state  $\eta$  evolves according to the master equation

$$\partial_t P(\eta) = [\lambda(\eta - 1)P(\eta - 1) - \lambda(\eta)P(\eta)] + [\mu(\eta + 1)P(\eta + 1) - \mu(\eta)P(\eta)], \tag{2.13}$$

where  $\lambda$  and  $\mu$  are the upward and downward rates of transition and have been chosen so that the dynamics of the original model are essentially recovered on average. In addition, a multi-cloud version of the skeleton model that also includes the effects of congestus and stratiform clouds has been recently developed by Thual and Majda (2015), though we focus here on the original first-baroclinic mode formulation that focuses on deep convection.

Solutions to the extended stochastic skeleton model were found numerically by Thual et al. (2015) with an idealized seasonally-varying warm pool background state. These solutions were found to exhibit several types of realistic convective events. In particular, three types of model convective events that correspond to observations were studied in detail: symmetric, half-quadrupole, and meridionally-tilted events; these tilted events were reminiscent of the BSISO.

All of these extended model solutions were found using idealized and equal forcing functions, i.e.  $S^{\theta} = S^{q}$ . The rest of this paper will be concerned with observation-based solutions to the extended model with  $S^{\theta}(x) \neq S^{q}(x)$ .

## 3 Data and Methods

We next construct estimates of the necessary background state  $\bar{A}$  and forcing terms  $S^{\theta}$  and  $S^{q}$  for the linear deterministic equations and the nonlinear stochastic model, respectively. The datasets and methods used here are similar to those of previous studies by the authors; additional details may be found in Stechmann and Majda (2015) and Ogrosky and Stechmann (2015a,b, 2016).

## 3.1 Datasets

NCEP/NCAR reanalysis daily surface latent heat net flux (Kalnay et al., 1996) and GPCP daily and monthly precipitation data (Huffman et al., 2012) are used to estimate the forcing terms  $S^{\theta}$  and  $S^{q}$  and the background state  $\bar{A}$ . The latent heat net flux has a spatial resolution of  $1.875^{\circ} \times 1.875^{\circ}$  and the GPCP data has a spatial resolution of  $1^{\circ} \times 1^{\circ}$ . Both datasets are interpolated here to a  $2.5^{\circ} \times 2.5^{\circ}$  spatial resolution.

The monthly precipitation data is available beginning in 1979, while the daily data is available beginning in October 1996. Since monthly data is available for a longer time period, the steady-state forcing functions used in the stochastic model were estimated using monthly data from 1 January 1979 through 31 December 2013. For all other uses here, including estimating observed variability, the daily data was used from 1 January 1997 through 31 December 2013. The seasonal averages of each variable are constructed for the June-July-August (JJA) season during the entire time periods used.

# 3.2 Estimating $S^q$ and $S^\theta$ for the nonlinear stochastic model

The moistening term  $S^q$  may be prescribed as in Ogrosky and Stechmann (2015a), where seasonal averages of reanalysis daily latent heat net flux were used. Specifically, this time-averaged latent heat flux data LHF(x, y) is projected onto the first ten meridional modes  $\phi_m(y)$  resulting in LHF $_m(x)$  for  $0 \le m \le 9$ ; each meridional mode LHF $_m(x)$  may be calculated by

$$LHF_m(x) = \int_{-\infty}^{\infty} LHF(x, y)\phi_m(y) \, dy, \qquad (3.1)$$

and the total latent heating approximated by the truncated expansion

$$LHF(x,y) \approx \sum_{m=0}^{9} LHF_m(x)\phi_m(y). \tag{3.2}$$

Each mode is made dimensionless using a scale factor as in Ogrosky and Stechmann (2015a),

$$S_m^q = H_{\text{LHF}_m} \cdot \text{LHF}_m, \tag{3.3}$$

where

$$H_{\text{LHF}_m} \approx \frac{\int_0^{P_E} \bar{H} \bar{A}_m \, dx}{\int_0^{P_E} \text{LHF}_m \, dx}.$$
 (3.4)

The data may also be smoothed in x by retaining only the first  $k_{max}$  Fourier modes and by reducing the amplitude of zonal variations through introduction of a parameter  $\beta$ ,

$$S_{m}^{q} = \hat{S}^{q}(0) + \beta \sum_{k=1}^{k_{max}} \left[ \hat{S}^{q}_{m}(k) \exp\left(\frac{2\pi i k x}{P_{E}}\right) + \hat{S}^{q}_{m}(-k) \exp\left(-\frac{2\pi i k x}{P_{E}}\right) \right], \tag{3.5}$$

as in Ogrosky and Stechmann (2015a). The parameter  $\beta$  has been added to ensure that local differences between  $S^q$  and  $S^\theta$  are small enough to produce a positive background state of convective activity in the model at every longitude; further discussion of the model's sensitivity to the value of this parameter is given in Ogrosky and Stechmann (2015a) for a single-meridional-mode truncation of the model.

One option for estimating  $S^{\theta}$  is to use the method of Ogrosky and Stechmann (2015a), which relied on OLR being a good estimate of total diabatic heating  $\bar{H}\bar{A}-S^{\theta}$ . This method was successfully used on both a model of the MJO and a model of the Walker circulation (Stechmann and Ogrosky, 2014). Here, however, the data is being considered over a wider range of latitudes than in these previous studies, and it is not clear whether OLR is a suitable proxy for convection over this range; for this reason we turn to a different approach.

We will estimate  $S^{\theta}$  with a crude method that makes use of our estimate of  $S^q$  and an estimate of  $\bar{H}\bar{A}$ . Specifically, solving the steady-state model solution (2.10) for  $S_m^{\theta}$  yields

$$S_m^{\theta} = \frac{(\tilde{Q} - 1)\bar{H}\bar{A}_m + S_m^q}{\tilde{Q}}.$$
(3.6)

An estimate of the background state of convective activity  $\bar{H}\bar{A}$  may be found in the following way. GPCP precipitation data is seasonally averaged resulting in a background state of precipitation  $\bar{P}(x,y)$  measured in mm day<sup>-1</sup>. To estimate  $\bar{A}$  we note that the energy released by precipitation at a given location may be expected to increase the temperature of the surrounding column of air at a rate (in K day<sup>-1</sup>) of

$$\bar{H}\bar{A} = \left(\frac{g\rho_w L_v}{p_0 c_p}\right) \bar{P},\tag{3.7}$$

where  $g=9.8~{\rm m~s^{-2}}$  is acceleration due to gravity,  $\rho_w=10^3~{\rm kg~m^{-3}}$  is the density of water,  $L_v=2.5\times10^6~{\rm J~kg^{-1}}$  is the latent heat of vaporization,  $p_0=1.013\times10^5~{\rm kg~m^{-1}~s^{-2}}$  is the mean atmospheric pressure at mean sea level,  $c_p=1006~{\rm J~kg^{-1}}$  is the specific heat of dry air at constant pressure, and where  $\bar{P}$  has been converted to have units of m day<sup>-1</sup>. Next, this background state  $\bar{A}(x,y)$  is projected onto the meridional modes  $\phi_m(y)$ ; an approximation of the background state may be made by truncating this expansion at  $m=M_{\bar{A}}$  and by including multiplicative factors  $\gamma_m$ ,

$$\bar{A}(x,y) \approx \sum_{m=0}^{M_{\bar{A}}} \gamma_m \bar{A}_m(x) \phi_m(y). \tag{3.8}$$

The factors  $\gamma_m \leq 1$  have been added since the smoothing with  $\gamma_m = 1$  for  $0 \leq m \leq M_{\bar{A}}$  can create locations (x,y) with locally negative mean background state, something that is clearly unphysical and an artifact of the spectral truncation; here we take  $\gamma_0 = 1$  and  $\gamma_m = 0.6$  for  $1 \leq m \leq M_{\bar{A}}$ . Fig. 1(a) shows the JJA seasonal background state after this truncation with  $M_{\bar{A}} = 9$ ; Fig. 1(b) shows the same background state but after a zonal Fourier mode truncation where only the first  $k_{max} = 10$  Fourier modes were retained.

Fig. 2 shows the resulting estimate of  $S^q$  and  $S^\theta$  during JJA using the background state shown in Fig. 1(b) and with  $k_{max} = 10$  and  $\beta = 0.1$  in (3.5). Of course, prescribing  $S^\theta$  in this fashion should result

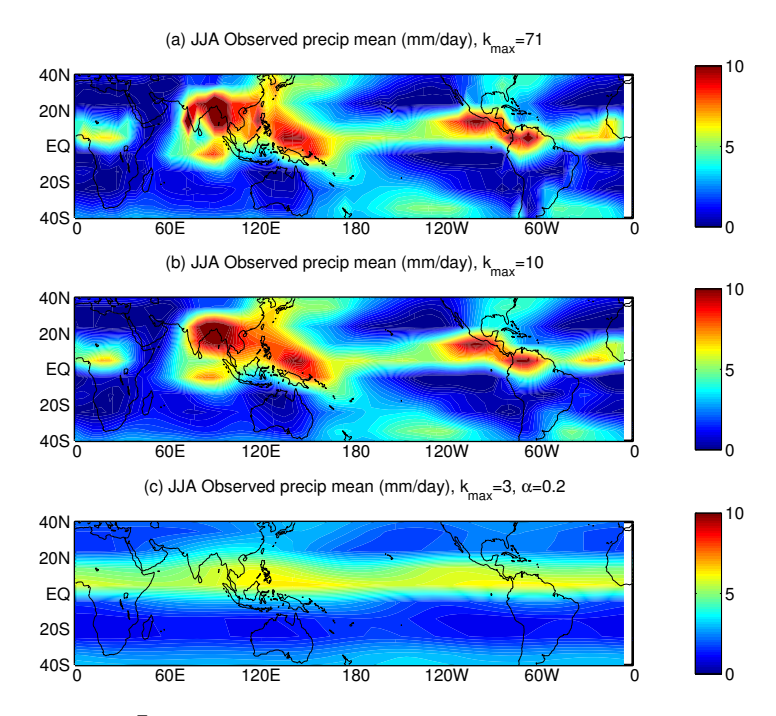


Fig. 1: (a) Background state  $\bar{A}$  estimated from GPCP data during the June-July-August (JJA) season with meridional mode truncation  $M_{\bar{A}}=9$ ;  $\gamma_0=1$  and  $\gamma_m=0.6$  for  $1\leq m\leq M_{\bar{A}}$  in (3.8), and  $k_{max}=71$  and  $\alpha=1$  in (3.9). (b) Same as (a) but truncated in the zonal direction for the nonlinear stochastic model with  $k_{max}=10$  and  $\alpha=1$ . (c) Same as (b) but with  $k_{max}=3$  and  $\alpha=0.2$ .

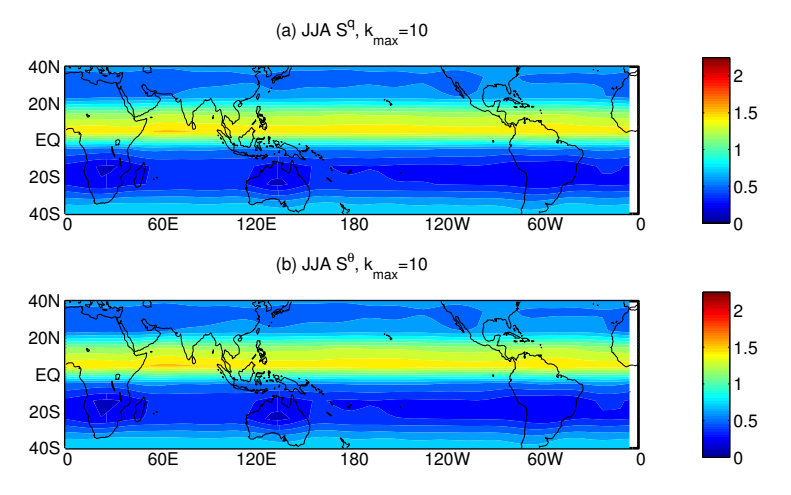


Fig. 2: (a) Background  $S^q$  estimated from latent heat flux. (b) Background  $S^{\theta}$  estimated from latent heat flux and precipitation (see text).

in the model's mean state closely resembling the observed background state; it will be shown in Sect. 4 that this is indeed the case. We note that the difference between  $S^q$  and  $S^\theta$  at any one location is small due to the factor  $(1-\tilde{Q})^{-1}$  in (3.6), consistent with previous studies of the skeleton model (Ogrosky and Stechmann, 2015a). We also note that other methods could be used to estimate  $S^\theta$  (see, e.g., L'Ecuyer and McGarragh (2010)).

## 3.3 Estimating forcing in the linear model

For the linear theory, the forcing functions are present in the model equations only through their effects on the background state  $\bar{A}$ . Thus, we may either prescribe the forcing functions, or directly prescribe a background state  $\bar{A}$ . Here we choose the latter approach and introduce one modification to the estimate of  $\bar{A}$  obtained above.

Prior to use in the linearized model, an additional smoothing of  $\bar{A}_m$  in x was performed by retaining only the first  $k_{max} = 3$  zonal Fourier modes, i.e.

$$\bar{A}_m(x) = \hat{A}_m(0) + \alpha \sum_{k=1}^{k_{max}} \left[ \hat{A}_m(k) \exp\left(\frac{2\pi i k x}{P_E}\right) + \hat{A}_m(-k) \exp\left(-\frac{2\pi i k x}{P_E}\right) \right], \tag{3.9}$$

where  $\hat{A}_m(-k) = [\hat{A}_m(k)]^*$  due to having a real-valued background state and where  $P_E$  is the dimensionless circumference of the Earth. The factor  $\alpha \leq 1$  reduces zonal variations in the background state and is added for two reasons. For one, as with the meridional truncation, Fourier filtering with  $\alpha = 1$  can again create locations with a negative mean background state. Second, as in Ogrosky and Stechmann (2015a), the eigenvectors of some of the linear solutions are very sensitive to zonal variations in the background state; using  $\alpha < 1$  results in solutions with a more realistic wave envelope. We use  $\alpha = 0.2$  in the results presented here unless specified otherwise; this smoothed background state is shown for the JJA season in Fig. 1(c).

# 3.4 Space-time filtering and power spectra

The stochastic model results will be analyzed using space-time filtering. This filtering will be used to isolate small zonal wavenumbers and intraseasonal frequencies; unless specified otherwise, only zonal wavenumbers  $|k| \le 3$  and frequencies  $\omega$  with  $1/90 \le \omega \le 1/10$  day<sup>-1</sup> are retained.

The logarithm of the wavenumber–frequency power spectrum of each model variable at a given latitude may be calculated using standard techniques as in, e.g., Wheeler and Kiladis (1999). After removing the mean from each variable at each spatial gridpoint, the ends of each time series are tapered to zero; the Fourier transform is then taken in both space and time, and the log of the square of the amplitude of the resulting Fourier coefficients is displayed for each  $(k, \omega)$  combination.

## 4 Stochastic model results

Next, the stochastic form of the skeleton model is studied. In Thual et al. (2015) the model was solved using equal forcing terms, i.e.  $S^{\theta} = S^q$ . Several forms of these forcing functions were studied including a warm pool with and without a seasonal cycle. Here, we use the estimates of JJA  $S^{\theta}$  and  $S^q$  shown in Fig. 2, and the use of  $S^{\theta} \neq S^q$  allows the formation of a Walker circulation.

The results presented here were produced with  $\Gamma=1.66$ . The extended model was solved using the numerical procedure described in Thual et al. (2015) and Thual and Majda (2015). The solver was run for 20,000 days, allowing for the model to settle into a statistical steady state.

# 4.1 Convective activity

Fig. 3 shows the mean and standard deviation of both the model convective activity  $\bar{H}A$  for a 10,000 day period of the simulation and GPCP precipitation data from 1 January 1997 through 31 December 2013. Both the simulation results and GPCP data were filtered so that only the first ten zonal wavenumbers k, i.e.  $|k| \leq 10$ , were retained prior to calculating the mean and standard deviation; the data was also filtered to retain only frequencies  $1/90 \leq \omega \leq 1/10$  day<sup>-1</sup> prior to calculating the standard deviation. The model mean convection agrees well with the observed mean precipitation, with a pattern correlation of 0.97; this agreement, of course, may be anticipated due to the method used for estimating  $S^{\theta}$ .

The model's standard deviation is also in reasonably good agreement with observed standard deviation, with a pattern correlation of 0.85, though the model exhibits higher-than-observed variability

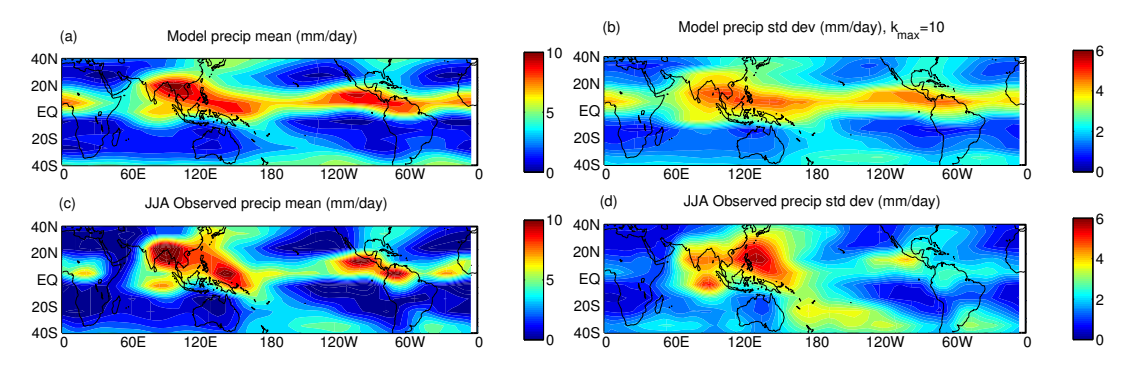


Fig. 3: (a) Long-time mean of model convective activity  $\bar{H}A$  with JJA forcing. (b) Model convective activity standard deviation with JJA forcing. (c) 1997-2013 mean JJA observed precipitation. (d) Observed standard deviation in daily JJA GPCP precipitation. All data filtered to retain zonal wavenumbers  $|k| \leq 10$ ; prior to calculating standard deviations, data filtered to retain frequencies  $1/90 \leq \omega \leq 1/10$  day<sup>-1</sup>.

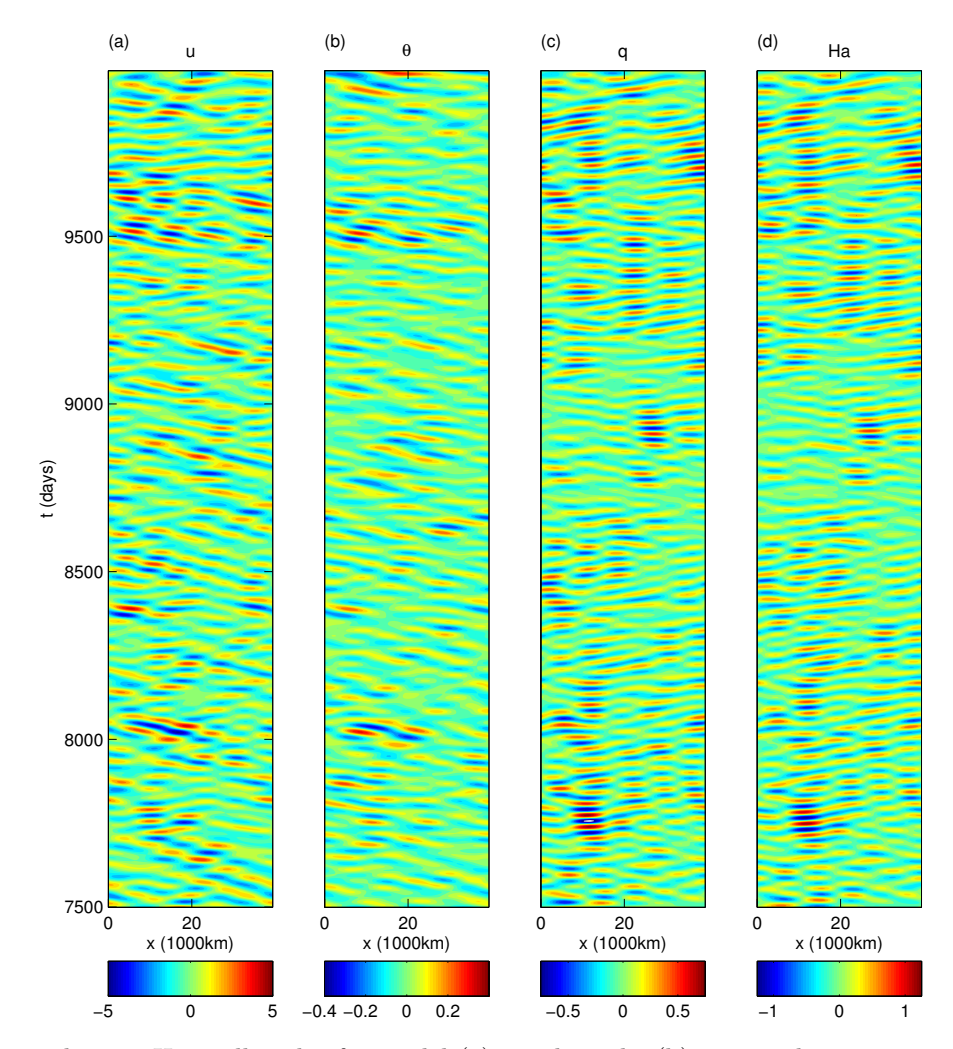


Fig. 4: Longitude-time Hovmoller plot for model (a) zonal winds, (b) potential temperature, (c) lower-tropospheric moisture, and (d) convective activity at 5N for two successive 2,000 day periods. Data filtered with  $|k| \leq 3$  and  $1/90 \leq \omega \leq 1/30$  day<sup>-1</sup>.

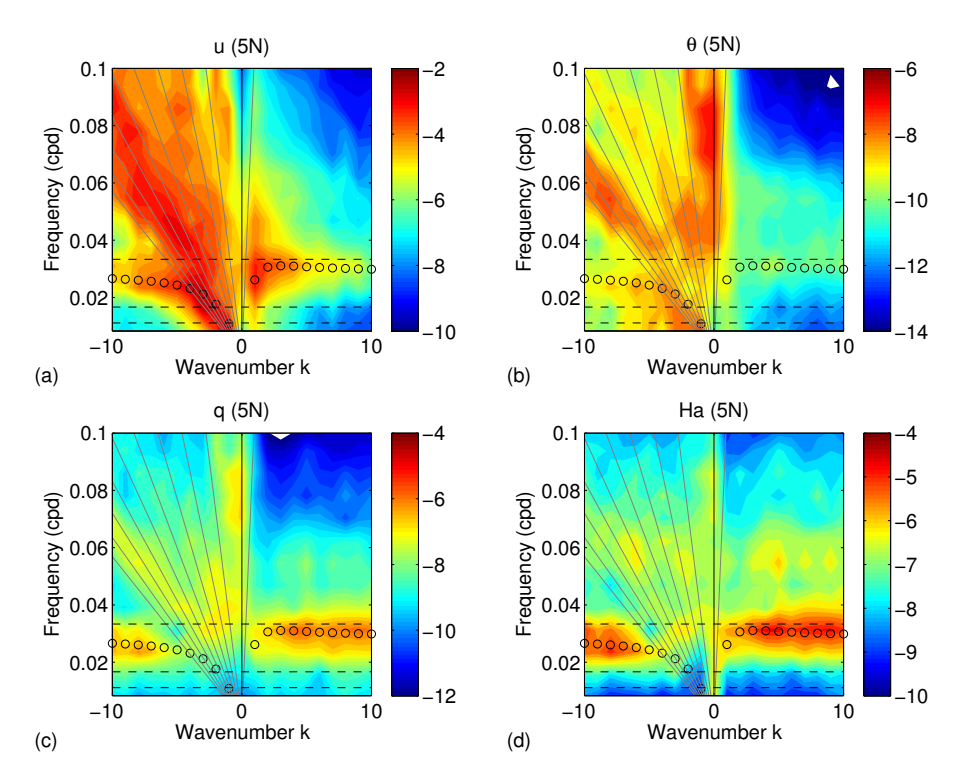


Fig. 5: Power spectrum for model (a) zonal winds, (b) potential temperature, (c) lower tropospheric moisture, and (d) convective activity at 5N for the time period depicted in Fig. 4(top). Dashed black lines indicate frequencies of 1/30, 1/60, and  $1/90 \, \mathrm{day}^{-1}$ , from top to bottom, respectively. Light grey lines denote dispersion relations of dry Kelvin and dry long-wave Rossby waves (m=1-10). Black circles denote the MJO and moist Rossby modes as in Ogrosky and Stechmann (2015a). Note that the colorbar has a different scaling for each variable.

over the eastern Pacific and the Congo, and lower-than-observed variability over the western Pacific in a region centered around 130E and 15N.

Fig. 4 shows a longitude-time Hovmoller diagram of anomalies of the model variables u,  $\theta$ , q and  $\bar{H}a$  for a 2,500 day period at 5N. The data have been filtered so that only wavenumbers  $k=\pm 1,\pm 2,\pm 3$  have been retained, and only frequencies  $1/90 \le \omega \le 1/30 \text{ day}^{-1}$  have been retained. The coupling between moisture and convection is apparent in Fig. 4. While both eastward and westward-moving events can be seen along with standing oscillations, eastward movement appears to occur more frequently than westward movement in both q and  $\bar{H}a$ . The dry variables u and  $\theta$  also exhibit both eastward and westward movement, but westward-moving anomalies appear to dominate their evolution, due perhaps in part to dry Rossby waves; see Chen et al. (2015) for a related model of interaction between dry Rossby waves and intraseasonal variability.

Fig. 5 shows the power spectrum of each variable and confirms the dominance of westward movement of zonal winds and potential temperature and eastward movement of moisture and convective activity apparent in Fig. 4. Zonal winds exhibit peaks lying along both moist Rossby and dry Rossby dispersion curves, with some eastward low-wavenumber intraseasonal power as well. Potential temperature anomalies occur primarily along dry Rossby dispersion curves. Moisture and convective activity exhibit primarily eastward-moving intraseasonal anomalies, with westward-moving power of weaker magnitude.

At subtropical latitudes, the dynamics are dominated by dry Rossby waves rather than intraseasonal convective activity. Fig. 6 shows the power spectrum of each variable at 24S. Moisture, zonal winds, and potential temperature all exhibit spectral peaks lying along dry Rossby curves, with potential temperature exhibiting much stronger anomalies at these latitudes than near the equator. There is much less power at all scales in convective activity at this latitude.

Next we examine meridional movement of convection. Fig. 7 shows a latitude-time Hovmoller diagram of the model's convective activity  $\bar{H}a$  at 90E for an 8000-day period; the data have been filtered with

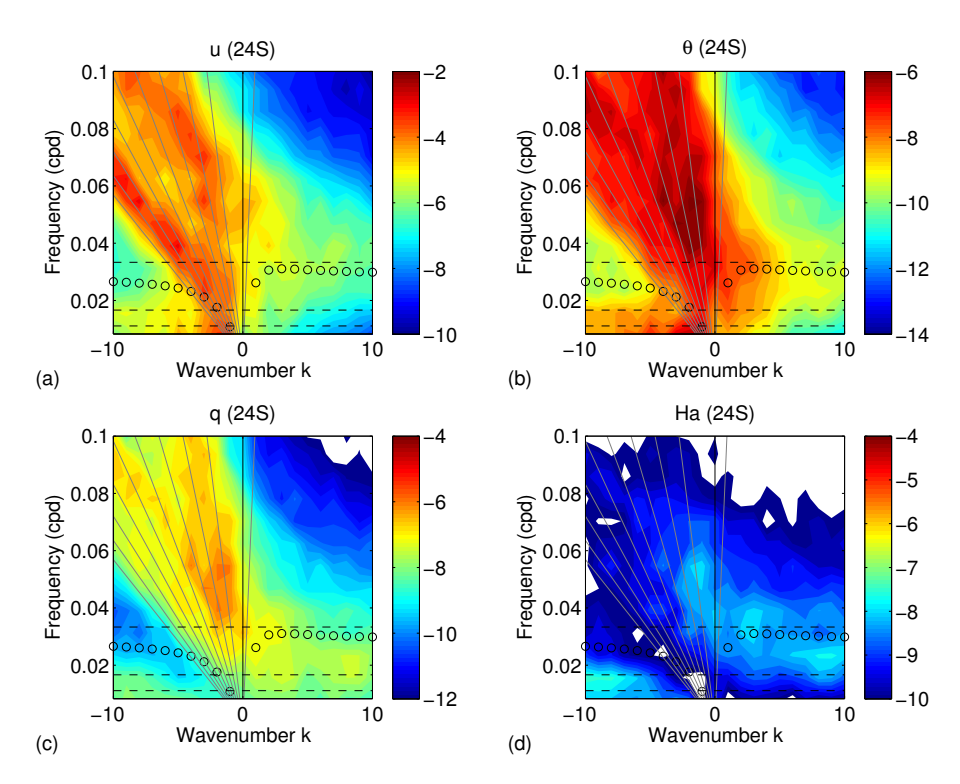


Fig. 6: Same as Fig. 5 but for model variables at 24S.

zonal wavenumbers  $|k| \leq 3$  and intraseasonal frequencies  $1/90 \leq \omega \leq 1/30$  day<sup>-1</sup> retained. The strongest anomalies are contained exclusively in a band of latitudes ranging from approximately 10S to 20N, consistent with the region of strongest moisture forcing. Both northward and southward moving events can be seen, though a slight preference appears to exist for northward-moving events, with the strongest of these occurring between day 9800 and day 9900; other instances of northward movement can be seen, e.g., during days 8500 through 8600 and days 10,500 through 10,600.

# 4.2 Individual events

We next examine a few individual cases of strong convective events in the model. While not exhaustive, these cases present some of the primary types of anomalies seen in model solutions. In particular, we discuss (i) a meridionally-tilted event with convection propagating both northwards and eastwards, (ii) an event with convection propagating primarily northwards, and (iii) an event propagating primarily eastwards.

Fig. 8 shows six snapshots of the model's convective activity beginning at day 7700 and ending at day 7725; the data has been filtered to retain only zonal Fourier coefficients  $|k| \leq 3$ . At day 7700, a strong convective event has formed along the equator centered in the Indian Ocean at approximately 90E. Between day 7700 and day 7715 the convective center strengthens and propagates both northwards and eastwards over parts of the maritime continent. From day 7715 to day 7725 the convective event center moves primarily eastward, lying north of the equator. A meridional tilt (northwest-southeast) somewhat similar to that seen in observations (Lawrence and Webster, 2002) is apparent throughout the evolution of this event. The northward and eastward movement of this event is consistent with Figs. 4 and 7.

A second event is also depicted in Fig. 8 with six snapshots of the model's convective activity beginning at day 9840 and ending at day 9859. At day 9840, a strong convective event exists in the eastern Indian Ocean and across the maritime continent with some weaker anomalies extending west-northwest from this center. Over the next twenty days, this convective event moves northward, reaching the Bay of Bengal and the subcontinent by day 9859. Some meridional tilt exists in the anomalies here as well, though the convective activity's movement is primarily northwards throughout this twenty day period;

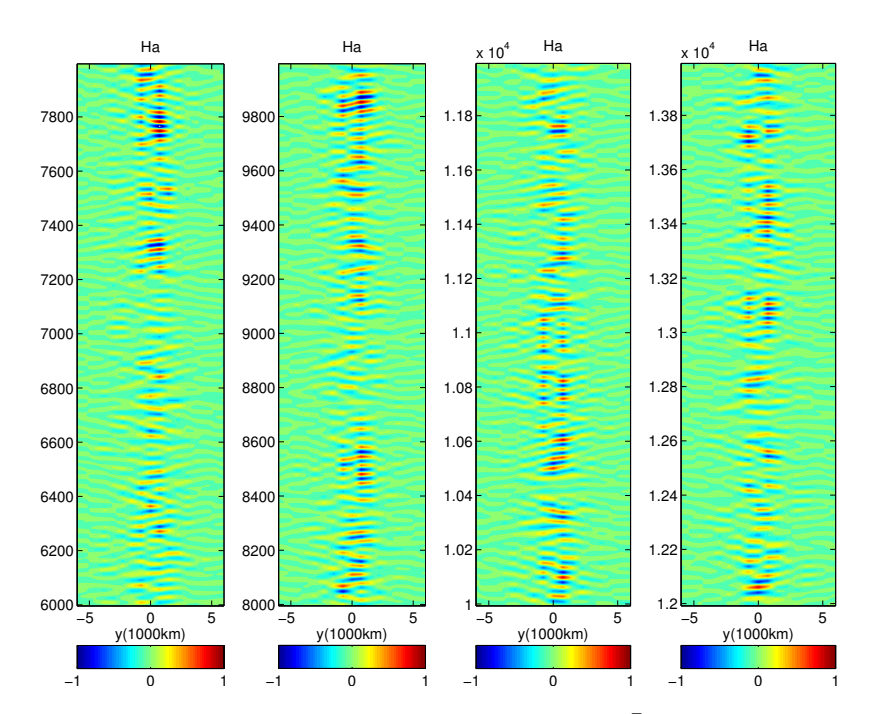


Fig. 7: Latitude-time Hovmoller plot for model convective activity  $\bar{H}A$  at 90E for an 8,000 day period. Data filtered with  $|k| \leq 3$  and  $1/90 \leq \omega \leq 1/30$  day<sup>-1</sup>.

this movement is again consistent with Figs. 4 and 7. In addition, there is significant intraseasonal convective activity occurring in the Eastern Pacific and propagating eastward across Central America.

A third event is depicted in Fig. 9, which shows six snapshots of the model's convective activity beginning at day 7741 and ending at day 7766. At day 7741, a center of convective activity is forming in the northern Indian Ocean. This center strengthens and moves primarily eastward at a latitude of approximately 10N, crossing the maritime continent and reaching the Date line by day 7766. While some meridional tilt can be seen in some of the snapshots, it is not a primary feature of the event, and its eastward movement with no corresponding northward movement is again consistent with Figs. 4 and 7.

# 5 Linear theory

The previous three examples of individual events are characteristic of much of the variability seen in the model. We next turn to the linear version of the model to explore the structure of its solutions.

Solutions to the linear version of the extended deterministic model given in (2.6a)-(2.6d) and (2.12) are found next for the truncation  $M_R = M_{\bar{A}} = 9$ . Each variable K,  $R_m$ ,  $Q_m$ , and  $A_m$  may be expressed as

$$K(x,t) = e^{-i\omega t} \sum_{k=-k_m}^{k_m} \hat{K}_k e^{2\pi i kx/P_E},$$
 (5.1)

where  $k_m$  is a chosen maximum wavenumber retained ( $k_m \ge 40$  in all results presented here). Substitution of (5.1), similar expressions for each of the  $R_m$ ,  $Q_m$ , and  $A_m$ , and the background state (3.9) into the linear equations results in a single system of  $(4+M_R+2M_A)(2k_m+1)$  equations for the Fourier coefficients  $\hat{K}_k$ ,  $\hat{R}_{m,k}$ , etc. The large number of equations to be solved simultaneously is due to the coupling across zonal wavenumbers through the background state  $\bar{A}_m$  in (2.12). We note that if  $M_R = M_A = 0$ , the equatorially-symmetric system considered in Ogrosky and Stechmann (2015a) is recovered.

The results presented here are for the value of  $\Gamma = 0.6$ . While this value of  $\Gamma$  is lower than that used in the nonlinear section ( $\Gamma = 1.66$ ), both of these values are consistent with values used for the stochastic and linear models in previous studies, respectively. In addition, it has been shown previously that the nonlinear stochastic form of the model tends to produce lower-frequency variability than the

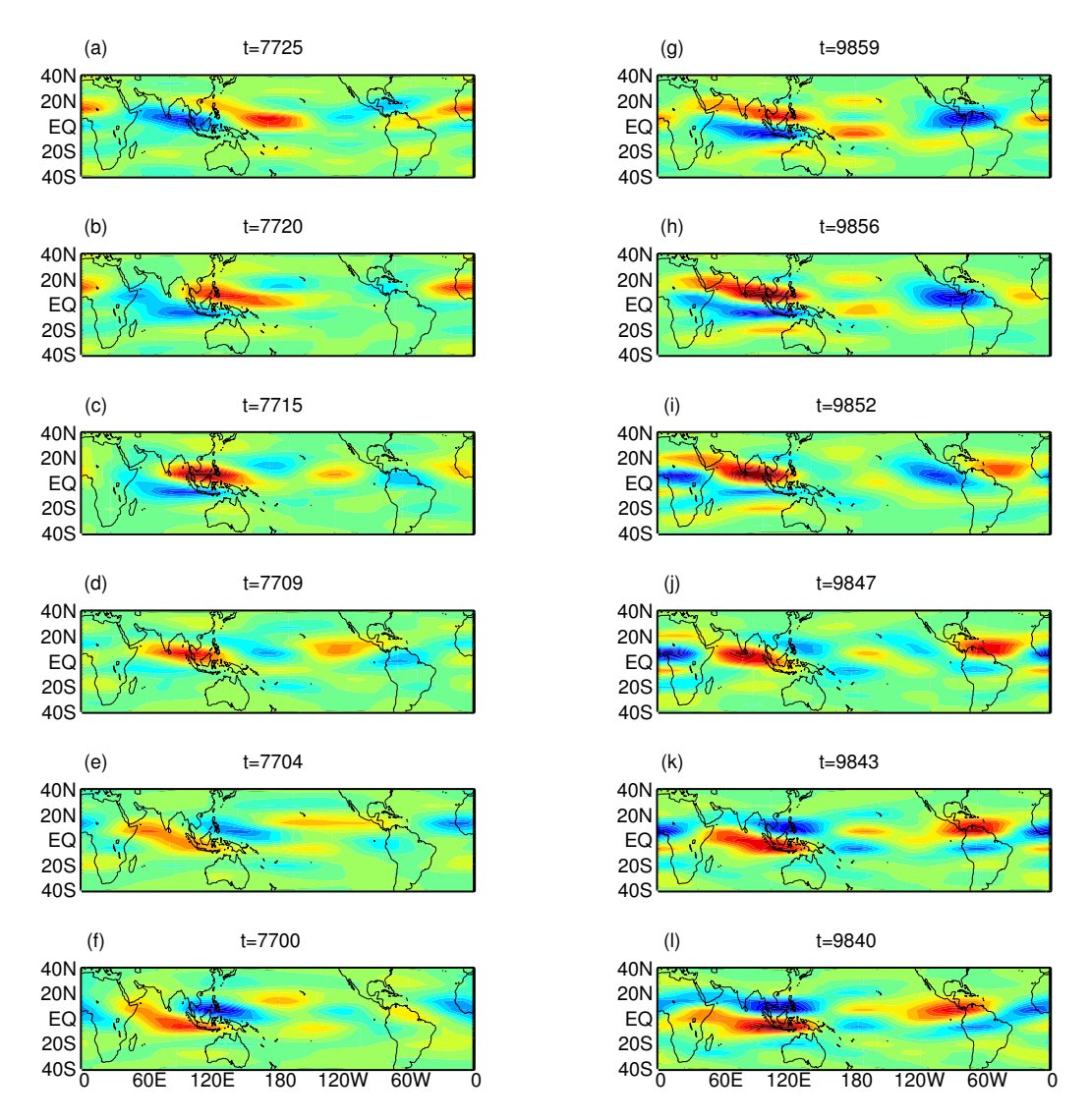


Fig. 8: (a)-(f) Tilted event with both northward and eastward propagation: Model convective activity  $\bar{H}A$  filtered by retaining zonal wavenumbers  $|k| \leq 3$  for six snapshots beginning on (f) day t = 7700 and ending on (a) day t = 7725. (g)-(l) Northward propagation: Same as (a)-(f) but beginning on (l) day t = 9840 and ending on (g) day t = 9859.

linear form of the model for identical parameter choices (Thual et al., 2014); here, in order to produce oscillations with similar frequencies to the nonlinear results, we opt to use  $\Gamma = 0.6$ .

The low-frequency (less than 1/20 day<sup>-1</sup>) eigenvalues of the linear system associated with a positive (eastward) phase speed are shown in Fig. 10, where the background state of Fig. 1(c) has been used. The system also has eigenvalues corresponding to dry Kelvin and Rossby modes with higher frequency as well as westward-moving low-frequency moist Rossby modes, but as the focus here is on intraseasonal variability which exhibits primarily eastward and northward movement, we will examine the low-frequency eastward-moving modes. The eigenvalues are here shown as a function of 'average wavenumber', where the average wavenumber of an eigenvalue's associated eigenvector is defined as

$$\bar{k} = \sum_{k=-k_m}^{k_m} |k| \left( \hat{K}_k^2 + \sum_{m=1}^{M_R+1} \hat{R}_{m,k}^2 + \sum_{m=0}^{M_A} \hat{Q}_{m,k}^2 + \sum_{m=0}^{M_A} \hat{A}_{m,k}^2 \right)^{1/2}.$$
 (5.2)

In Fig. 10, the two modes (out of the first eight) with lowest average wavenumber  $\bar{k}$  that exhibit significant tropical convective activity are denoted by blue circles. The other six modes out of the first eight

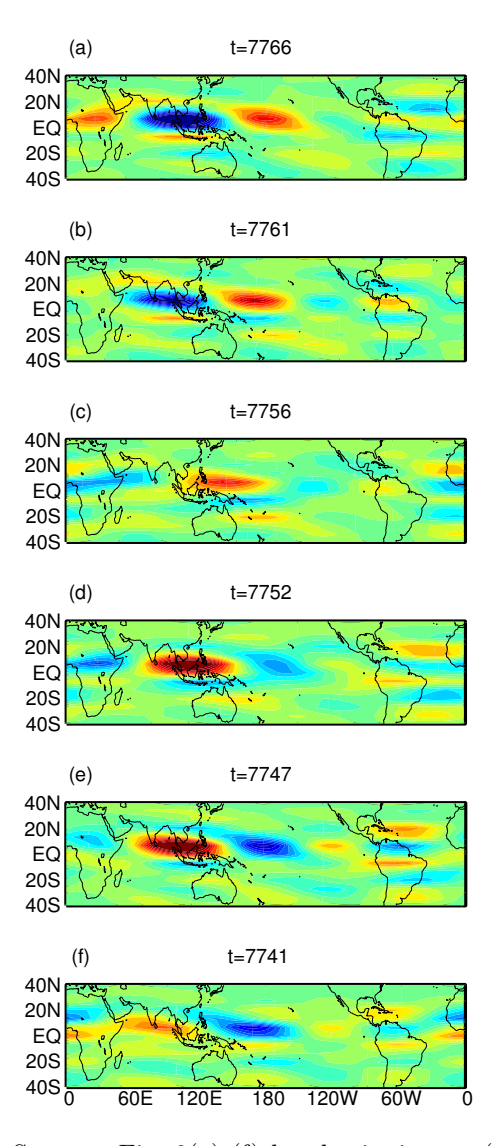


Fig. 9: Eastward propagation: Same as Fig. 8(a)-(f) but beginning on (f) day t = 7742 and ending on (a) day t = 7767.

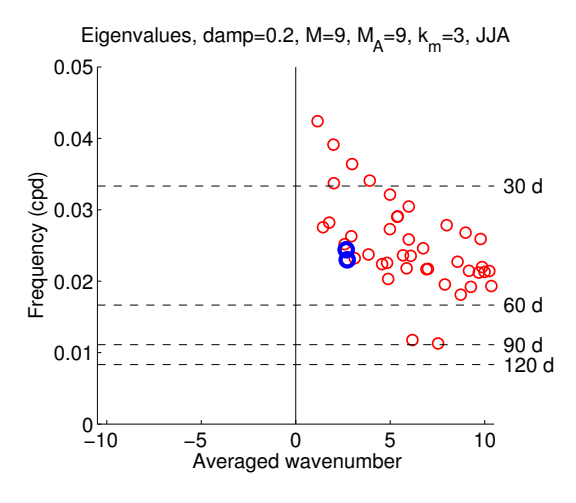


Fig. 10: Eigenvalues corresponding to slow eastward-moving solutions (red circles) with  $M_R = M_A = M_{\bar{A}} = 9$  and with  $k_m = 40$ . Bold blue circles denote modes shown in Fig. 11.

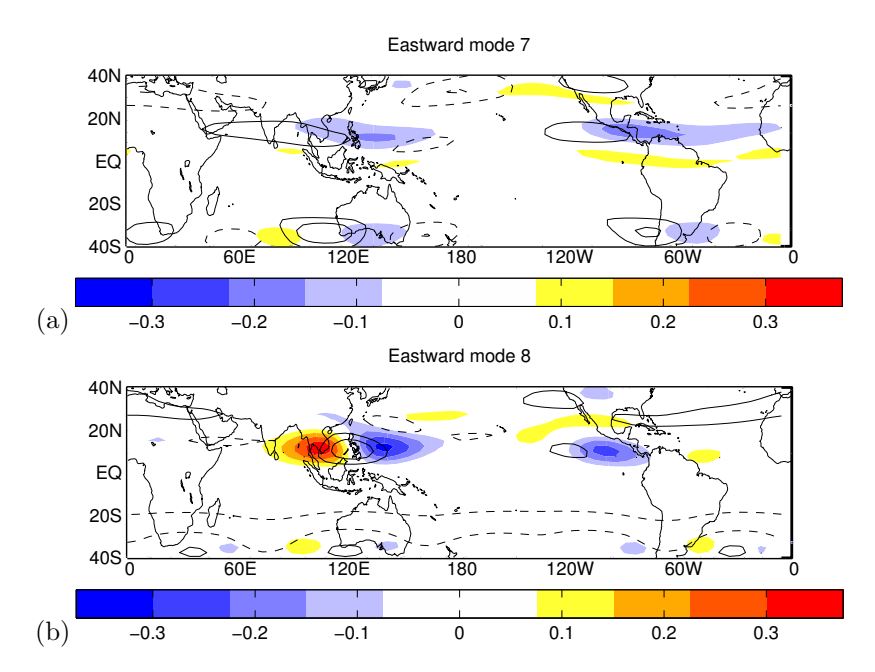


Fig. 11: The two slow eastward-moving modes with lowest average wavenumber  $\bar{k}$  that exhibit significant tropical convective activity. Convective anomalies are depicted by shading; positive (negative) moisture contours are depicted by solid (dashed) lines. For mode 7,  $\omega = 0.024$  cycles day<sup>-1</sup>,  $\bar{k} = 2.7$ ; for mode 8,  $\omega = 0.023$  cycles day<sup>-1</sup>,  $\bar{k} = 2.7$ .

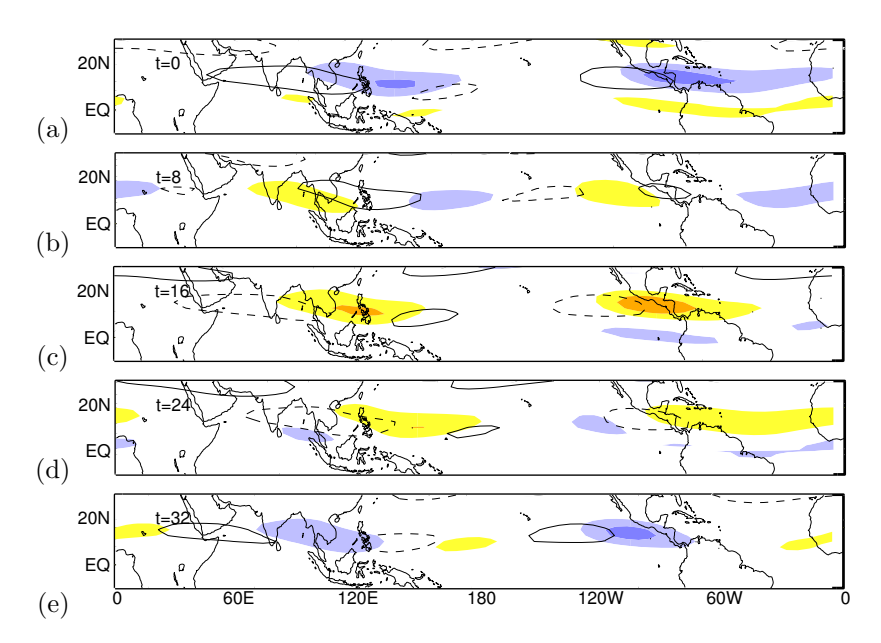


Fig. 12: Propagation of eastward mode 7 from Fig. 11; (a) t = 0, (b) t = 8 days, (c) t = 16 days, (d) t = 24 days, (e) t = 32 days.

exhibit convective activity primarily well outside the tropics. As the focus of the current study is tropical intraseasonal variability, we focus on modes with significant tropical convective activity and discuss their properties next.

Fig. 11 shows a snapshot of the anomalies in convective activity and moisture associated with each of these modes. Consistent with the skeleton model's premise and solutions found previously, lower-tropospheric moisture anomalies lead convective anomalies in these eastward-moving modes. Both modes show convective anomalies between 10N and 20N and 90E and 150E, near the area where the BSISO is

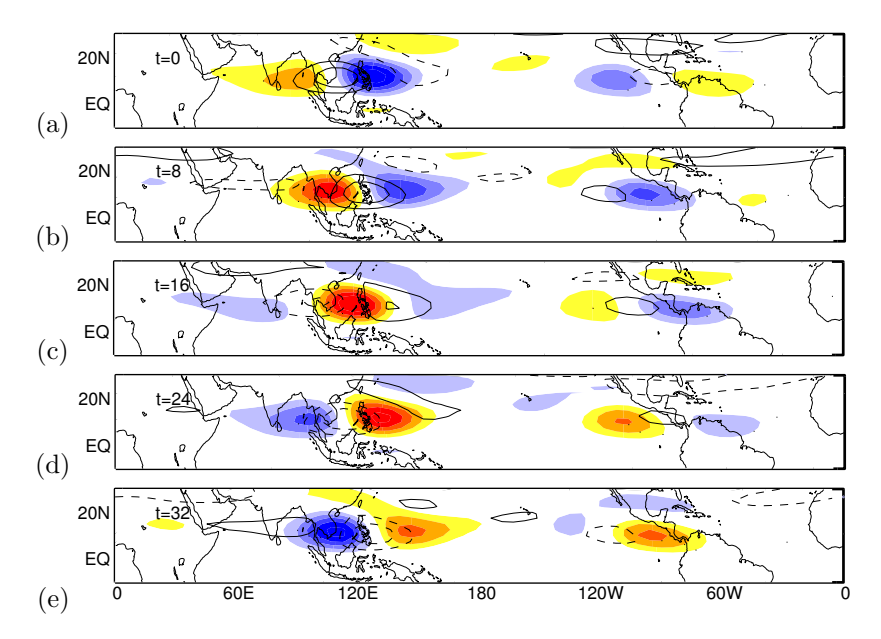


Fig. 13: Propagation of eastward mode 8 from Fig. 11; (a) t = 0, (b) t = 8 days, (c) t = 16 days, (d) t = 24 days, (e) t = 32 days.

most active. A meridional (northwest-southeast) tilt can be seen in the convective activity of mode 7; this tilt is somewhat reminiscent of the tilt seen by Lawrence and Webster (2002). Very slight tilts can also be seen in mode 8. Additional convective anomalies can be seen in each mode between 10N and 20N near Latin America.

We next consider the propagation of each mode's tropical convective anomalies. Fig. 12 shows the evolution of mode 7. Convective anomalies can be seen forming in the Indian ocean just north of the equator at approximately 90E. These anomalies grow into a meridionally-tilted band which propagates eastward reaching maximum strength near 120E. Due to both the expansion of the region of convective activity and its tilt, precipitation at a fixed longitude (e.g., 90E) appears to move northward from Day 0 to 16, similar to many observed BSISO events in, e.g., Lawrence and Webster (2002). Convective anomalies are also seen over the eastern Pacific and Latin America, strongest between 10N and 20N and 120W and 60W, and their eastward movement is similar to that seen in composites of intraseasonally-filtered rainfall and OLR in this region (Maloney and Kiehl, 2002; Jiang et al., 2013, 2014). The 15-day lag between convective activity over the Indian ocean and over the eastern Pacific found by Yu et al. (2011), however, is not seen in mode 7, where the convection in the two regions is close to being in-phase.

The evolution of mode 8 is shown in Fig. 13. The convective activity that grows and decays primarily between 60E and 180 is somewhat reminiscent of the boreal winter MJO, only displaced northwards so that the strongest anomalies occur between 10N and 20N. As with mode 7, there is significant variability located over the eastern Pacific and Latin America with propagation similar to observations but without the observed lag correlation with variability in the eastern hemisphere.

Next we consider the degree to which convection associated with each of these modes propagates in a north-south direction. A latitude-time Hovmoller plot of these modes each at three different longitudes is shown in Fig. 14. Mode 7 shows evidence of northward movement of convection at all three longitudes considered (approximately 80E, 100E, and 125E). The northward movement of this activity occurs at approximately 1 m s<sup>-1</sup>, which is within the 1-2.5 m s<sup>-1</sup> northward phase speed range found in Lawrence and Webster (2002). Mode 8 shows much less north-south propagation of convection, though some evidence of northward movement of convection from 20N to near 30N can be seen at 124E.

Lastly, we examine east-west propagation of convection in each mode. A longitude-time Hovmoller plot of convection at three latitudes, EQ, 10N, and 20N, is shown in Fig. 15. Not surprisingly, both modes show eastward movement, though at different speeds. Mode 7 propagates at approximately 5 m  $\rm s^{-1}$ , in good agreement with eastward moving variability seen in Lawrence and Webster (2002), though we note that the strongest convective activity here occurs at a higher latitude range (10N to 15N) than found in their study (0 to 5N). Mode 8 propagates more slowly at approximately 2.5 m  $\rm s^{-1}$ .

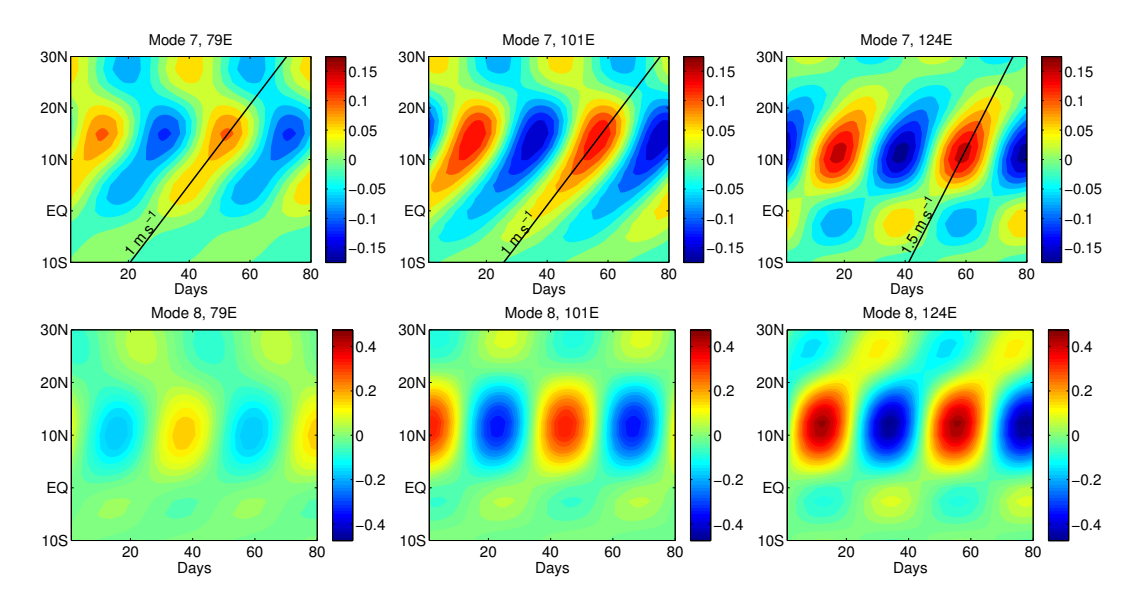


Fig. 14: Latitude-time Hovmoller plots of convective anomalies  $\bar{H}a$  of modes 7 and 8 from Fig. 11 at (left) 79E, (middle) 101E, and (right) 124E.

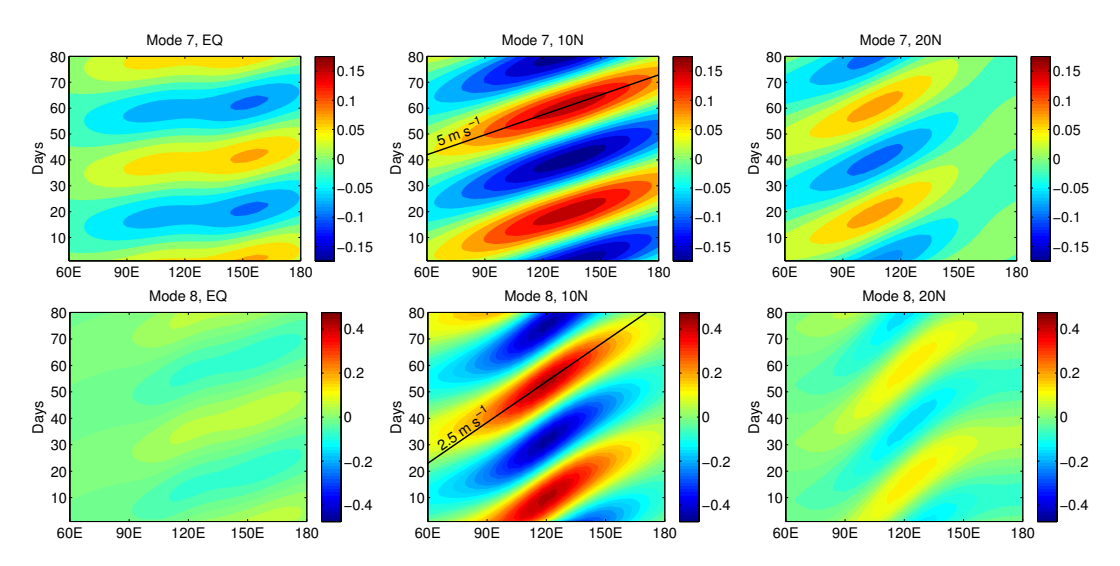


Fig. 15: Longitude-time Hovmoller plots of convective anomalies  $\bar{H}a$  of modes 7 and 8 from Fig. 11 at (left) the equator, (middle) 10N, and (right) 20N.

# 6 Parameter sensitivity study

Before concluding, we briefly discuss the sensitivity of the results presented here to choices in the model's parameter values and mode truncation.

There are several choices that must be made in truncating the linear model:  $M_A$ , the number of meridional modes of convective activity to retain; and  $M_{\bar{A}}$  and  $k_{max}$ , the number of meridional and zonal modes of the background state to retain, respectively. The model was solved for various values of each of these truncation parameters, including every combination of  $0 \le M_A \le 9$  and  $0 \le M_{\bar{A}} \le 9$  with  $k_{max} = 0$ . For a fixed value of  $M_{\bar{A}}$ , increasing  $M_A$  results in (i) slight modification of existing eigenvalues and their associated eigenvectors, and (ii) the introduction of additional eigenvalues. Likewise, for a fixed value of  $M_A$ , increasing  $M_{\bar{A}}$  results in eigenvalues and eigenvectors that are only slightly modified. Thus none of these changes were found to significantly alter the structure and propagation of the solutions of interest. For  $k_{max} > 0$ , the changes to the eigenvalues remain small, but the eigenvectors corresponding to intraseasonal frequencies undergo significant changes due to the coupling between zonal wavenumbers

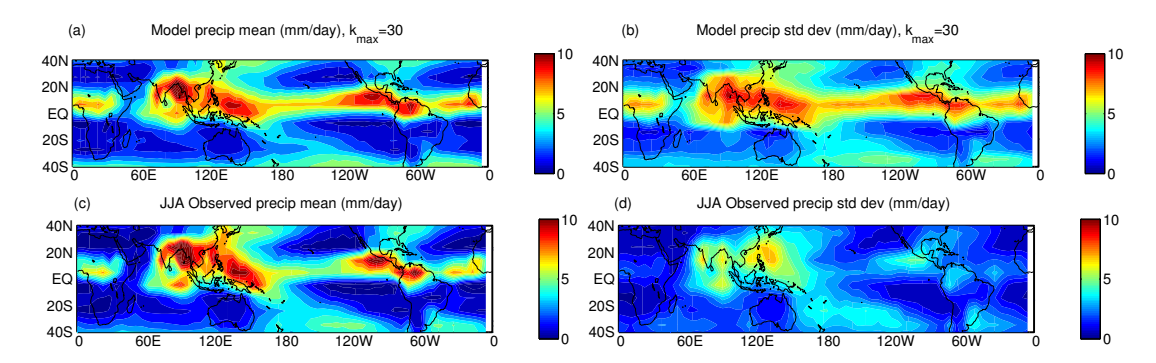


Fig. 16: Same as Fig. 3 but with data filtered to retain zonal wavenumbers  $|k| \leq 30$ .

through the background state. The same behavior was observed with  $M_A = M_{\bar{A}} = 0$  in Ogrosky and Stechmann (2015a), and is one of the reasons for the parameter  $\alpha$  introduced in (3.9).

As the skeleton model was designed to describe the planetary-scale dynamics, all of the results presented here have made use of only a few zonal wavenumbers of the background state and forcing functions, i.e.  $k_{max} \leq 3$ . We next discuss stochastic model results for higher values of  $k_{max}$  which push the limits of the validity of the planetary-scale skeleton model, but are perhaps worth trying due to the smaller spatial scale of the BSISO than its boreal winter counterpart, the MJO. Fig. 16 shows the mean and standard deviation for model convective activity with  $k_{max} = 30$  and the corresponding observed quantities. The model mean and observed mean exhibit very good agreement. The model standard deviation and observed standard deviation exhibit similar spatial patterns, though the model has larger standard deviation than the observations almost everywhere.

Results have been presented here for the linear model with  $\Gamma=0.6$  and for the stochastic model with  $\Gamma=1.66$ ; both the linear and stochastic versions of the model were run with other values of the growth/decay rate parameter  $\Gamma$  as well. When the stochastic model is run with  $\Gamma=0.6$ , for example, the results are largely identical, at least qualitatively, to those given here, though the model's slight preference for northward propagation of convection appears to be weaker, if it exists at all, with this smaller value of  $\Gamma$ .

## 7 Conclusions

To conclude, an extended form of the skeleton model for intraseasonal variability has been studied using observation-based estimates of the JJA background state and forcing terms. The model produces reasonably realistic intraseasonal variability throughout the tropics, and solutions to two forms of the model, a linear deterministic version and a nonlinear stochastic version, are able to produce convective events reminiscent of the BSISO.

The stochastic model produces a wide variety of convective events, including meridional tilts and propagation similar to the BSISO. The spatial pattern of some of these events, and their propagation, are reminiscent of the observed BSISO. Solutions to the linearized model contain events that exhibit a meridional (northwest-southeast) tilt as well as northward and eastward propagation of convection. Both the eastward and northward movement occurs at speeds lying within the range established by previous observational studies (Lawrence and Webster, 2002). This convective activity is also associated with convection in other parts of the tropics including over the eastern Pacific in reasonable agreement with observational studies (Maloney and Kiehl, 2002; Jiang et al., 2013, 2014). It would be interesting to examine the skeleton model's ability to reproduce other types of intraseasonal oscillations; this question is left to future work.

Acknowledgments: The data for this paper are available from NOAA/OAR/ESRL/PSD, Boulder, Colorado, USA, from their website at http://www.esrl.noaa.gov/psd/. The research of A.J.M. is partially supported by ONR MURI Grant N00014-12-1-0912. The research of S.N.S. is partially supported by ONR Young Investigator Award N00014-12-1-0744, ONR MURI Grant N00014-12-1-0912, and by the Sloan Research Fellowship. H.R.O. is supported as a postdoctoral researcher by ONR MURI Grant N00014-

12-1-0912. The authors thank Sulian Thual for the numerical solver used to solve the stochastic skeleton model.

## References

- Ajayamohan RS, Khouider B, Majda AJ (2014) Simulation of monsoon intraseasonal oscillations in a coarse-resolution aquaplanet GCM. Geophys Res Lett 41:5662-5669.
- Ajayamohan RS, Goswami BN (2007) Dependence of simulation of boreal summer tropical intraseasonal oscillations on the simulation of seasonal mean. J Atmos Sci 64:460-478.
- Chen S, Majda AJ, Stechmann SN (2015) Multiscale asymptotics for the skeleton of the Madden-Julian oscillation and tropical–extratropical interactions. Math Clim Weather Forecast 1:43-69.
- Gill AE (1980) Some simple solutions for heat-induced tropical circulation. Quart J R Meteorol Soc 106:447-462.
- Hendon HH, Salby ML (1994) The life cycle of the Madden-Julian oscillation. J Atmos Sci 51:2225-2237. Huffman GJ, Bolvin DT, Adler RF (2012) GPCP Version 2.2 SG Combined Precipitation Data Set. WDC-A, NCDC, Asheville, NC. Data set accessed 12 February 2014 at http://www.ncdc.noaa.gov/oa/wmo/wdcamet-ncdc.html.
- Jiang X, Maloney ED, Li J-LF, Waliser DE (2013) Simulations of the Eastern North Pacific intraseasonal variability in CMIP5 GCMs. J Clim 26:3489-3510.
- Jiang X, Kubar TL, Wong S, Olson WS, Waliser DE (2014) Modulation of marine low clouds associated with the tropical intraseasonal variability over the Eastern Pacific. J Clim 27:5560-5574.
- Kalnay E, Kanamitsu M, Kistler R, Collins W, Deaven D, Gandin L, Iredell M, Saha S, White G, Woollen J, Zhu Y, Chelliah M, Ebisuzaki W, Higgins W, Janowiak J, Mo KC, Ropelewski C, Wang J, Leetmaa A, Reynolds R, Jenne R, Joseph D (1996) The NCEP/NCAR 40-year reanalysis project. Bull Am Meteorol Soc 77:437-471.
- Kikuchi, K, Wang B, Kajikawa Y (2012) Bimodal representation of the tropical intraseasonal oscillation. Clim Dvn 38:1989-2000.
- L'Ecuyer TS, McGarragh G (2010) A 10-year climatology of tropical radiative heating and its vertical structure from TRMM observations. J Clim 23:519-541.
- Lawrence DM, Webster PJ (2002) Boreal summer intraseasonal oscillation: relationship between northward and eastward movement of convection. J Atmos Sci 59:1593-1606.
- Lee J-Y, Wang B, Wheeler MC, Fu X, Waliser DE, Kang I-S (2013) Real-time multivariate indices for the boreal summer intraseasonal oscillation over the Asian summer monsoon region. Clim Dyn 40:493-509.
- Lin J-L, Kiladis GN, Mapes BE, Weickmann KM, Sperber KR, Lin W, Wheeler MC, Schubert SD, Del Genio A, Donner LJ, Emori S, Gueremy J-F, Hourdin F, Rasch PJ, Roeckner E, Scinocca JF (2006) Tropical intraseasonal variability in 14 IPCC AR4 climate models. Part I: convective signals. J Clim 19:2665-2690.
- Madden RA, Julian PR (1971) Detection of a 40-50 day oscillation in the zonal wind in the tropical Pacific. J Atmos Sci 28:702-708.
- Majda AJ (2003) Introduction to PDEs and waves for the atmosphere and ocean. Courant Lecture Notes in Mathematics. American Mathematical Society, Providence, RI, Vol 9.
- Majda AJ, Klein R (2003) Systematic multiscale models for the tropics. J Atmos Sci 60:393-408.
- Majda AJ Stechmann SN (2009) The skeleton of tropical intraseasonal oscillations. Proc Natl Acad Sci USA 106:8417-8422.
- Majda AJ, Stechmann SN (2011) Nonlinear dynamics and regional variations in the MJO skeleton. J Atmos Sci 68:3053-3071.
- Maloney ED, Hartmann DL (2000) Modulation of eastern north Pacific hurricanes by the Madden-Julian oscillation. J Clim 13:1451-1460.
- Maloney ED, Kiehl JT (2002) MJO-related SST variations over the tropical Eastern Pacific during Northern hemisphere summer. J Clim 15:675-689.
- Matsuno T (1966) Quasi-geostrophic motions in the equatorial area. J Meteorol Soc Japan 44:25-42.
- Myers DS, Waliser DE (2003) Three-dimensional water vapor and cloud variations associated with the Madden-Julian oscillation during Northern hemisphere winter. J Clim 16:929-950.
- Ogrosky HR, Stechmann SN (2015a) The MJO skeleton model with an observation-based background state and forcing. Quart J Roy Meteorol Soc 141:2654-2669.

- Ogrosky HR, Stechmann SN (2015b) Assessing the equatorial long-wave approximation: asymptotics and observational data analysis. J Atmos Sci 72:4821-4843.
- Ogrosky HR, Stechmann SN (2016) Identifying convectively coupled equatorial waves using theoretical wave eigenvectors. Mon Weather Rev 144:2235-2264.
- Sperber KR, Kim D (2012) Simplified metrics for the identification of the Madden-Julian oscillation in models. Atmos Sci Lett 13:187-193.
- Stachnik JP, Waliser DE, Majda AJ, Stechmann SN, Thual S (2015) Evaluating MJO event initiation and decay in the skeleton model using an RMM-like index. J Geophys Res 120:11486-11508.
- Stechmann SN, Majda AJ (2015) Identifying the skeleton of the Madden-Julian oscillation in observational data. Mon Weather Rev 143:395-416.
- Stechmann SN, Ogrosky HR (2014) The Walker circulation, diabatic heating, and outgoing longwave radiation. Geophys Res Lett 41:9097-9105.
- Szekely E, Giannakis D, Majda AJ (2015) Extraction and predictability of coherent intraseasonal signals in infrared brightness temperature data. Clim Dyn 46:1473-1502.
- Szekely E, Giannakis D, Majda AJ (2016) Initiation and termination of intraseasonal oscillations in nonlinear Laplacian spectral analysis-based indices. Math Clim Weather Forecast 2:1-25.
- Thual S, Majda AJ, Stechmann SN (2014) A stochastic skeleton model for the MJO. J Atmos Sci 71:697-715.
- Thual S, Majda AJ, Stechmann SN (2015) Asymmetric intraseasonal events in the MJO skeleton model with seasonal cycle. Clim Dyn 45:603-618.
- Thual S, Majda AJ (2015) A suite of skeleton models for the MJO with refined vertical structure. Math Clim Weather Forecast 1:70-90.
- Wang B, Rui H (1990) Synoptic climatology of transient tropical intraseasonal convection anomalies: 1979-1985. Meteorol Atmos Phys 44:43-61.
- Wheeler MC, Hendon HH (2004) An all-season real-time multivariate MJO index: development of an index for monitoring and prediction. Mon Weather Rev 132:1917-1932.
- Wheeler MC, Kiladis GN (1999) Convectively coupled equatorial waves: analysis of clouds and temperature in the wavenumber–frequency domain. J Atmos Sci 56:374-399.
- Yu W, Han W, Maloney ED, Gochis D, Xie S-P (2011) Observations of eastward propagation of atmospheric intraseasonal oscillations from the Pacific to the Atlantic. J Geophys Res 116:D02101.
- Zhang C (2005) Madden-Julian oscillation. Rev Geophys 43:RG2003.